Materials Characterization 183 (2022) 111639

Contents lists available at ScienceDirect

Materials Characterization

journal homepage: www.elsevier.com/locate/matchar

Effect of the nanostructuring by high-pressure torsion process on the secondary phase precipitation in UNS S32750 Superduplex stainless steel

Alisiya Biserova-Tahchieva [a,*], Dipanwita Chatterjee [b], Antonius T.J. van Helvoort [b], Núria Llorca-Isern [a], Jose Maria Cabrera [c]

[a] Universitat de Barcelona, Departament de Ciència de Materials i Química Física, Martí i Franquès 1-10, 08028 Barcelona, Spain
[b] Norwegian University of Science and Technology, Department of Physics, Høgskoleringen 5, Natural Science Building, 7034, Trondheim, Norway
[c] Universitat Politècnica de Catalunya, EEBE, Dept. Ciència dels Materials i Enginyeria Metal·lúrgica, 08019 Barcelona, Spain

ARTICLE INFO

Keywords:
Superduplex stainless steel
HPT
Severe plastic deformation
Phase precipitation

ABSTRACT

In this work, the precipitation and the morphology of secondary phases after severe plastic deformation (SPD) processing followed by an isothermal treatment was investigated. High-pressure torsion (HPT) was the SPD process carried out on superduplex 2507 (UNS S32750) stainless steel material under $P = 6$ GPa at room temperature. At this high strain levels (ε up to 170) samples have shown grain size decrease and strained microstructure with high dislocation density and nanostructure features. After a short isothermal treatment at 830 °C, the sigma phase and chromium nitrides were revealed as the main secondary phases identified by scanning and transmission electron microscopy and element analysis by energy dispersive spectroscopy. Scanning precession electron diffraction and automated crystal orientation mapping have been carried out in order to confirm the precipitation of the secondary phases. In fact, the results provide evidence that the precipitation of chromium nitrides seems to be the preferred nucleation site for sigma phase at higher deformation strain, in addition to the intergranular precipitation of sigma. Both the sigma phases nucleated integranularly and besides chromium nitrides are randomly orientated.

1. Introduction

The global demand for high-performance stainless steels will continue to increase as stainless steels have a significant impact environmentally and economically. Despite the exploitation of the renewable energies and other sources of energy that are increasing continuously, oil and gas industries will still have to search for materials operative at the reservoirs that are both geologically challenging and have operational complexities [1]. In order to satisfy these demands and many others in the chemical engineering, offshore structures and constructions, duplex stainless steels will still be used as they combine excellent properties. For instance, they show better toughness and corrosion resistance, as well as higher strength than the austenitic stainless steels [2]. At the same time, their cost is also lower than that of austenitic stainless steels due to the low content of Ni. Combining ferrite (δ) and austenite (γ) phases in equal proportion satisfies the increased requirement in yield strength and corrosion resistance that cannot be found in just ferritic or austenitic stainless steels alone. Therefore, a huge range of demands is expected for other diverse applications as well. For example, in the nuclear plants, reactor design is currently studied with the aim to explore, among other solutions, the control of the steel microstructure evolution. Also, here the formation of secondary phases is of crucial importance. Microstructural changes involve the formation of brittle secondary phases or undesirable intermetallic precipitates, among which sigma (σ) phase is one of the most significant [3–9]. Sigma phase is investigated mainly for its influence on the impact toughness and corrosion susceptibility due to the Cr-depleted zones [10,11]. Chromium nitrides (CrN, Cr_2N) or carbides ($M_{23}C_6$, M_7C_3) also may precipitate, especially in grades with higher amount of nitrogen during aging [6], [12–16] that can affect the mechanical properties of the material. Thus, critical alloying elements such as Cr, Mo and Ni decompose and lead to the decrease of the mechanical and corrosion properties. The most studied precipitates involve σ precipitation mechanism into the ferrite phase and chromium nitrides at γ/δ, γ/γ and δ/δ interfaces. Thorough investigation of their morphology and size [17–18], the precipitation mechanism [19] and the orientation

* Corresponding author.
E-mail address: abiserova.tahchieva@ub.edu (A. Biserova-Tahchieva).

https://doi.org/10.1016/j.matchar.2021.111639
Received 21 July 2021; Accepted 27 November 2021
Available online 1 December 2021

relationship between precipitates and the matrix has been carried out and reported in literature [20–21]. However, most of these studies consider the microstructure of the steels directly after conventional deformation processes, or after industrial processing steps and aging processes without taking into account any other previous procedures affecting the changes in their microstructure. For example, processing the steel to obtain an ultrafine grained microstructure lead to greater mechanical properties of toughness, strength and fatigue resistance [22]. Some of these grain size refinement procedures include the severe plastic deformation (SPD) methods and are considered as more effective than conventional plastic deformation ones [23–24]. One of the processes of SPD that does greatly retain the dimensions of the object is the high-torsion pressure (HPT) process. It allows the formation of nanostructures that show significant increase in mechanical properties and most importantly, in superplasticity without the addition of any other alloying element as reported by Maehara [25]. Moreover, as a mechanical procedure for microstructure refinement and thereby the improvement of mechanical properties, it is very interesting to study the influence of such deformation on the thermodynamically induced changes in the microstructure. However, this combined approach is hardly covered by publications in this subject yet. The aim of this work is to investigate the microstructural evolution in UNS S32750 superduplex stainless steel material deformed through the HPT process at room temperature and its influence on the precipitation process after an isothermal treatment carried out to the processed samples. The ultrafine grains and precipitates are examined by field-emission scanning electron microscopy (FE-SEM) and transmission electron microscopy (TEM) using both conventional and the scanning precession electron diffraction technique (SPED). The main advantage of precession is the removal of the strong dynamical effects of diffraction [26]. By obtaining kinematical diffraction patterns with a greater number of spots and even intensities, the data analysis process is easier and useful for automated crystal orientation mapping (ACOM). Thereby, phase mapping and orientation mapping can be done as common in EBSD [27]. Here SPED technique and sequential ACOM data analysis have been used to identify the secondary phases and their orientation within the biphasic matrix.

2. Materials and methods

2.1. Materials and samples

Superduplex stainless steel grade 2507 (UNS S32750) was the material used for this study with the chemical composition balanced in Fe shown in Table 1. Disc-shaped samples of 10 mm diameter and 1 mm thick were cut along the length of a hot extruded tube. Thermo-Calc software [28] was used to simulate the fraction of equilibrium phase versus temperature in thermodynamic conditions through the steel database TCFE8.

2.2. Experimental procedure

All samples were solution annealed at 1080 °C for 30 min in order to remove any undesirable phases and homogenise the structure and then water-quenched prior to the deformation. HPT process was unconstrained and carried out at room temperature under the pressure of $P = 6$ GPa at different numbers of full revolutions (labelled as "turns", $N = 1$, 5 and 10) with a rotation speed of 1 rpm. The samples were placed one by one between a pair of anvils, strained by pressing them and rotating the lower anvil (schematic representation of the process and the aspect of the samples is shown in Fig. 1 (c)). After that, samples were submitted to isothermal treatment in order to cause the precipitation of secondary phases. Samples were heated up to 830 ± 5 °C for around 3 min and rapidly water-quenched.

All SEM micrographs in the current study are representative from the edge of the processed samples, where the strain is higher, according to the strain equation:

$$\gamma = 2\pi rN/h \quad (1)$$

being r the radius of the disc, N the number of HPT turns and h the final thickness of the sample. The equivalent strain, is then calculated as stated by Von Mises equation:

$$\varepsilon = \gamma/\sqrt{3} \quad (2)$$

This equation is useful for strains $\gamma \leq 0.8$. When $\gamma \geq 0.8$, the thickness is taken into consideration and the equivalent strain is as stated in (5), proposed by [34,35].

$$\varepsilon = ln\left(\frac{2\pi Nrh_0}{h^2}\right) \quad (3)$$

Sample nomenclature/labelling and the equivalent strain for each sample calculated at 3.5 mm from the center of the disc samples by eqaution (2) and (3) are shown in Table 2. However, in many cases, making reference to the number of HPT turns is more common in order to avoid confusion about the induced strain when comparing different studies [35].

2.3. Samples preparation

After HPT processing, cross-sectional (TD) samples were polished using abrasive papers and diamond suspension, successively, down to 1 μm in order to obtain a mirror-like surface aspect for microstructure characterization by SEM. TEM thin foils were prepared by mechanical grinding up to ~1 mm thickness, then a careful mechanical polishing further thinned them to ~30 μm thickness by using different diamond lapping films (Pace Technologies) from 30 μm to 1 μm. A final step was to thin the sample to electron transparency using Dual Ion Milling System (Fischione Instruments) operating at 5 kV acceleration voltage, starting with an initial incidence milling angle of 10° and reduced to 5° before the foil/specimen perforation.

2.4. Microstructural characterization

Field-emission scanning electron microscope - JEOL J-7100F (JEOL Ltd., Tokyo, Japan) with a coupled Robinson back scattered electron (BSE) detector was used. BSE imaging mode was applied as it is more sensitive to compositional variations (heavier elements appear brighter, lighter elements appear darker). Thus,identification of the different phases was done easily. Energy dispersive X-ray spectroscopy (EDS, 80 mm^2 SDD, Oxford Instrument AZtec) was used for the chemical composition verification once different phases were identified based on BSE contrast variations. At least 5 points were verified for the same crystal. The obtained composition through BSE FESEM-EDS is considered qualitatively, particularly for the small deleterious phases which were difficult to detect by the electron probe size.

A JEOL JEM 2100 and JEOL 2100F (JEOL Ltd., Tokyo, Japan) - *located at Centres Científcs i Tecnològics de la Universitat de Barcelona (CCiTUB) and at theTEM Gemini Centre, respectively* -operated at acceleration voltage of 200 kV, both equipped with EDS system (80 mm^2 SDD, Oxford Instruments AZtec) and the commercial precession system

Table 1
Nominal chemical composition of UNS S32750, balanced in Fe.

Alloy	C	Si	Mn	P	S	Cr	Ni	Mo	N	Cu
2507	0.018	0.26	0.84	0.019	0.001	25.08	6.88	3.82	0.29	0.17

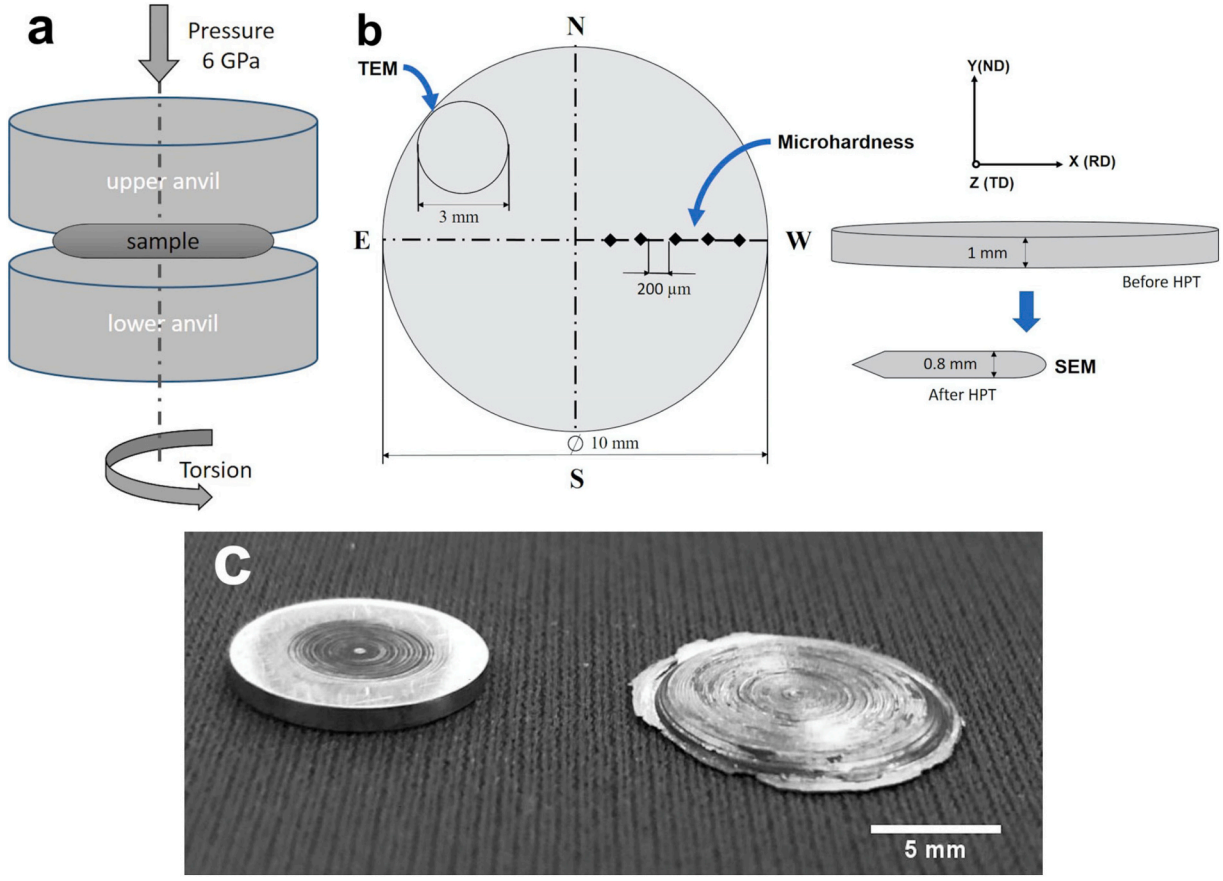

Fig. 1. (a) Schematic illustration of HPT process, (b) sample characterization and microhardness measurements sketch, (c) sample aspect before (left) and after (right) 10 turns HPT.

Table 2
Samples labelling with HPT number of turns and after the isothermal treatment. Equivalent strain for each sample calculated at 3.5 mm from the center of the disc samples.

HPT turns (N)	After HPT	After HPT and the isothermal treatment	$\varepsilon = \gamma/\sqrt{3}$	$\varepsilon = ln\left(\frac{2\pi N r h_0}{h^2}\right)$
N = 0	MS0	MST0	$\varepsilon = 0$	$\varepsilon = 0$
N = 1	MS1	MST1	$\varepsilon = 15$	$\varepsilon = 3.5$
$N = 5$	MS5	MST5	$\varepsilon = 80$	$\varepsilon = 5$
$N = 10$	MS10	MST10	$\varepsilon = 160$	$\varepsilon = 6$

DigiSTAR tool and an external StingRay CCD by NanoMegas. The process consists of setting the TEM in the scanning precession electron diffraction (SPED) mode. The incident electron beam is scanned over the area of interest due to the deflecting coils of TEM by an external control system. Precession angles in the range of 0.2°-1° were used and exposure time at each location of 20 ms was set. The samples were firstly analyzed through scanning transmission electron microscopy (STEM) in order to detect precipitate elements in the different areas at a non-zone axis condition. The collected 4D SPED stacks of electron diffraction patterns were analyzed using INDEX (NanoMegas) software package to obtain phase and orientation maps. In this approach, a library of template kinematic diffraction patterns were generated using the crystal structure information of the different phases and the crystal orientations and phases were obtained through cross-correlation template matching technique of the experimentally acquired diffraction patterns [29]. The crystallographic data for each candidate phase (.CIF file) are presented in Table 3.

Table 3
Crystallographic data for each phase used as .cif file in the indexation process.

Phases	Lattice type	Space group (Laue class)
Austenite, **γ**	FCC	Fm3m [30]
Chromium nitrde, Cr_2N	Trigonal	P31m [31]
Sigma, **σ**	Tetragonal	$P4_2/mnm$ [32]

No additional image processing, such as, background subtraction or filtering was applied to the produced maps. The quality of indexation from the template matching is quantified by the image correlation index Q(i) for every template (4), which is a quantitative estimation of the matching and is highly sensitive to the external features like the foil thickness [33].

$$Q(i) = \frac{\sum_{j=1}^{m} [\![P(x_j,]\!]\ y_j)\, T_i(x_i, y_j)}{\sqrt{\sum_{j=1}^{m} [\![P^2(x_j,]\!]\ y_j)}\ \sqrt{\sum_{j=1}^{m} [\![T_i^2(x_k,]\!]\ y_j)}}, \quad (4)$$

where P(x,y) is the pattern intensity function and $T_i(x,y)$ is the template function. The highest Q value is closest to the solution. The orientation reliability (OR) of the suggested solution can be quantified by the ratio of the matching indices for the two best solutions Q1 and Q2 (5), which is ranges between 0 (two equivalent solution) and 100 (unique solution).

$$OR = 100\left(1 - \frac{Q_2}{Q_1}\right) \quad (5)$$

where Q1 and Q2 refer to two orientations of the selected phase. The brighter the pixel in the reliability maps, the more reliable the index-

ation is. Good indexation solutions should be with index and reliability higher than 500 and 40%, respectively. Full matching option was applied for the final maps.

2.5. Hardness measurements

Microhardness tests were performed with Galileo ISO-SCAN OD microhardness tester applying 0,981 N during 15 s. Hardness values were obtained from annealed and deformed samples and before and after the isothermal treatment. Measurements were done along the diameter of the samples and hardness indentations were taken at every 200 μm, as shown in the schematic in Fig. 1 (b).

3. Results

3.1. Equilibrium phase diagram

Fig. 2 shows the equilibrium phase diagram for the SDSS 2507 material, obtained from Thermo-Calc TCEF8 database. The mole fraction of the equilibrium phases in the range of 600 and 1200 °C are presented. It is noticeable that above 1050 °C only ferrite and austenite are stable, reaching an equivalent part of each at around 1150 °C. Therefore, the 1080 °C annealing treatment carried out for the experiments of this study ensures the homogeneity of the microstructure of the samples. The σ phase and Cr_2N (HCP) phase presented here are stable below ~1020 °C and below ~980 °C, respectively. Chromium carbides, $M_{23}C_6$, are hardly visible in the diagram, but very small amounts of carbide is predicted to be stable below around ~820 °C. The calculated results for the stability of the secondary phases are similar to the other diagram phases calculated for S2507 [36]. However, several data in the literature shows to have found χ phase to be stable at around 800 °C [37]. δ-ferrite is however not stable between 630 °C and 980 °C, as shown in the diagram. Therefore, it is expected to be absent in this temperature range.

3.2. Microstructure analyses by SEM and EDS

BSE images from FESEM presented in Fig. 3 (a) – (d) show the microstructure of the sample before deformation ($N = 0$). As seen, in all the four micrographs, different contrasts from different phases are observed. Ferrite is darker than austenite. Deleterious phases were identified as much brighter phases than the matrix (sigma assigned as σ and chi as χ are the brighter white phases). Their identification was verified by EDS compositional analyses. Both σ and χ have higher amounts of Cr and Mo than in ferrite and in addition to that, χ phase has higher Mo content [6]. EDS spectrum for σ is presented below in Fig. 3 (e). Precipitation of dark small phases were assigned to Cr_2N, after confirming the presence of nitrogen in the EDS spectrum, presented in Fig. 3 (f), as well. The precipitation of σ and Cr_2N is in accordance with the calculated Thermo-calc diagram (Fig. 2). The precipitation of χ phase was not identified by the equilibrium diagram shown. However, it is worth mentioning that the precipitation of such phases (as seen in Fig. 3) is not significant in the present samples. Moreover, χ phase is not stable at temperatures above 800 °C, as stated by other researchers for the same or similar duplex stainless steel alloy. Also, ferrite phase is not stable at 830 °C as seen in the equilibrium diagram (Fig. 2), but it has been detected in the cooled samples.

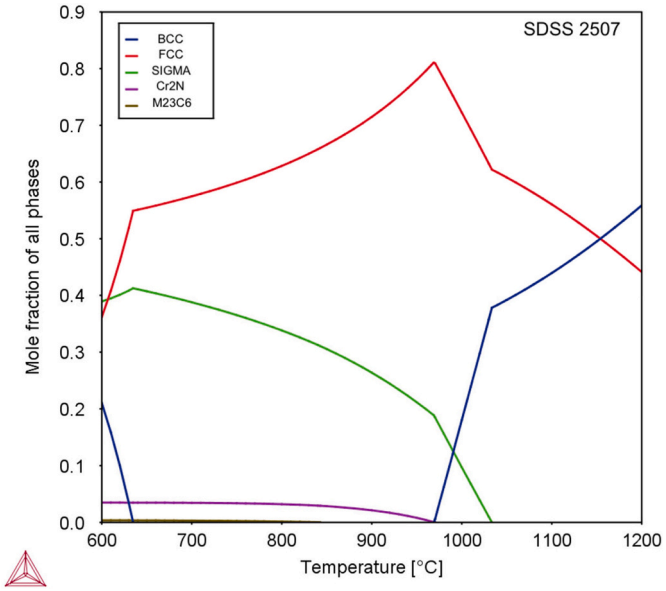

Fig. 2. Mole fraction vs. temperature equilibrium phase diagram of SDSS 2507.

Fig. 4 shows the microstructure of SDSS samples (a) MST1, (b) and (c) MST5 and (d) MST10, respectively. Grain size decrease with HPT turns is clearly observed. In addition, different magnifications of each micrograph are shown in order to see properly the precipitated dark phases. It is clearly seen that the precipitation of secondary phases is increased in comparison to the non-deformed sample (Fig. 3). As seen in Fig. 4 and in other experiments from literature [17], [38–40], σ precipitated preferentially at the austenite/ferrite interface and grow into the ferrite matrix until its total consumption. Different points marked in Fig. 4(b) have been analyzed. Table 4 shows the EDS analysis of the chemical composition of the marked pointsand no ferrite is found to be present (Point 1 corresponds to Cr_2N, Point 2 to σ, and Point 3 to austenite). A depleted zone in Cr and increased in Ni is analyzed between σ and austenite phases (Point 4). As mentioned previously, the micrographs are taken from the edge of the disc, where theoretically, the highest deformation was achieved. Therefore, the smaller grains with higher density of grain boundaries and interfaces appear. Thus, the highest amount of precipitates is observed in the sample with 10 HPT turns. However, Fig. 4 (c) shows a micrograph representative from the central part of the disk after 5 turns HPT, where less or no deformation is expected to be induced, according to Von Misses equation. In this zone, the precipitation of σ is detected, consuming all of the ferrite as also seen at the edge of the sample. In all the three samples, σ phase follows the cellular morphology precipitation, with the so-called secondary austenite γ_2, in between, which will be discussed later.

As depicted from Fig. 4, the grain size refinement increased with the HPT turns. Due to the limited spatial resolution in SEM, it becomes harder to determine the smaller phases, such as Cr_2N, between grain or phase boundaries. Thus, TEM investigation with different modes was performed.

3.3. Microstructure by conventional TEM

The deformed and isothermally treated samples were investigated with TEM. In Fig. 5, bright-field TEM images show MST1 (a) and (b), MST5 (c) and MST10 (d) samples with nearly the same grain size distribution (100–500 nm). In all the three samples the same precipitates were identified: intermetallic σ phase and Cr_2N. White arrows in Fig. 5 (d) point towards the high density of dislocation accumulation within/at grain boundaries in fcc-austenite grains.

3.4. Secondary phase identification through STEM/SPED

SPED mode in the TEM was used to index an area pixel by pixel containing the precipitates identified previously by STEM-EDS analyses. Thus, a correlative EDS and SPED measurement/study has been used for the identification of phases and analysis of their orientation relationships. Moreover, grain size and nucleation sites of the precipitates, grain boundaries and substructures could be identified/located from the indexed images.

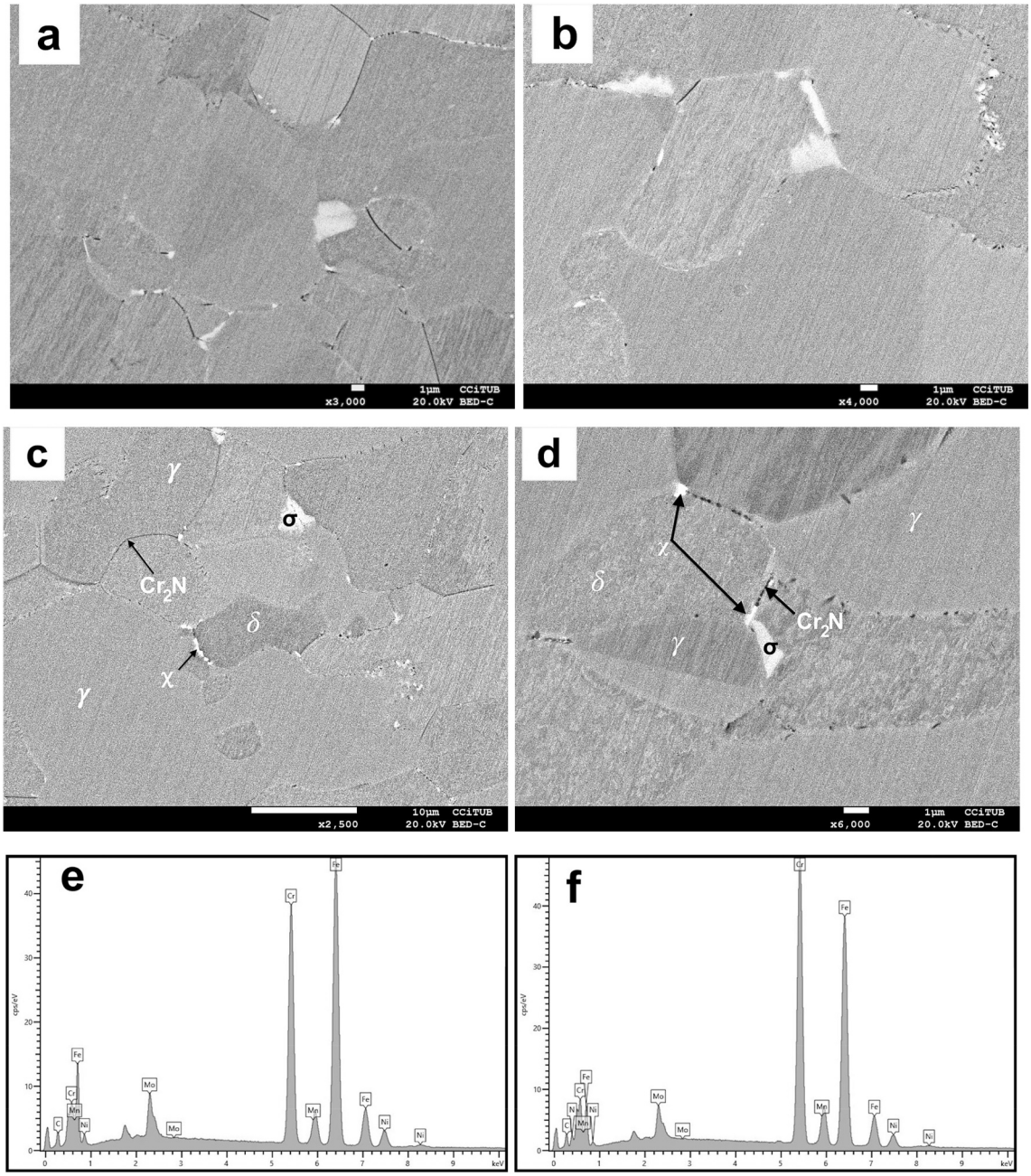

Fig. 3. (a)-(d) BSE FE-SEM micrographs of the MST0 sample, showing precipitation of σ, χ and Cr_2N . EDS spectra of (e) σ and (f) chromium nitride, marked in (d).

3.4.1. Scanning transmission electron microscopy(STEM)-EDS analyses of the deformed and isothermally treated samples

STEM-EDS was used to detect the areas with higher %wt in Cr, Mo and N and correlate them to the secondary phases. An area of interest with different grain morphologies was scanned and an increment of Cr, Mo in some of the grains was observed, suggesting those grains to be σ phase. The presence of Cr and N in some other grains also indicated a correlation to Cr_2N. Fig. 6 (b) shows the STEM-EDS distribution of the main elements to distinguish between phases in the MST1 sample. Bright field TEM image of a representative area is shown in Fig. 6 (a), where it is noticeable that different grain sizes are present. From very fine grains in the range of 80 to 100 nm to larger grain of 500 nm of irregular shapes are observed. Moreover, some strained grains full of dislocation boundaries can be observed (as was also observed in Fig. 5) which are fcc-austenite grains due to HPT deformation process done previously to the isothermal treatment. Grains without any sign of deformation or dislocations correspond to post isothermal treatment formation. Fig. 7 (a) and Fig. 8 (a) show large areas of the MST5 and MST10 samples along with their STEM-EDS elemental mapping, Fig. 7 (b)-(f) and Fig. 8 (b)-(f), respectively. Acknowledging the limitations of EDS as a measurement tool for accurate composition analysis, it is worth mentioning that these analyses were still helpful for narrowing down the possibilities of phases present in the microstructure. This knowledge was later used for the template matching in the SPED analysis.

3.4.2. Scanning precession electron diffraction analysis of deformed and isothermally treated sample MST1

Fig. 9 (a) and (b) show virtual bright-field image and the obtained indexed image of MST1, respectively. Three phases are identified in the scanned area of MST1. These phases are presented in the all three phase map in Fig. 9 (c) (cyan colour corresponds to austenite phase, purple to Cr_2N and green to σ phase). The phases observed at the austenite grain

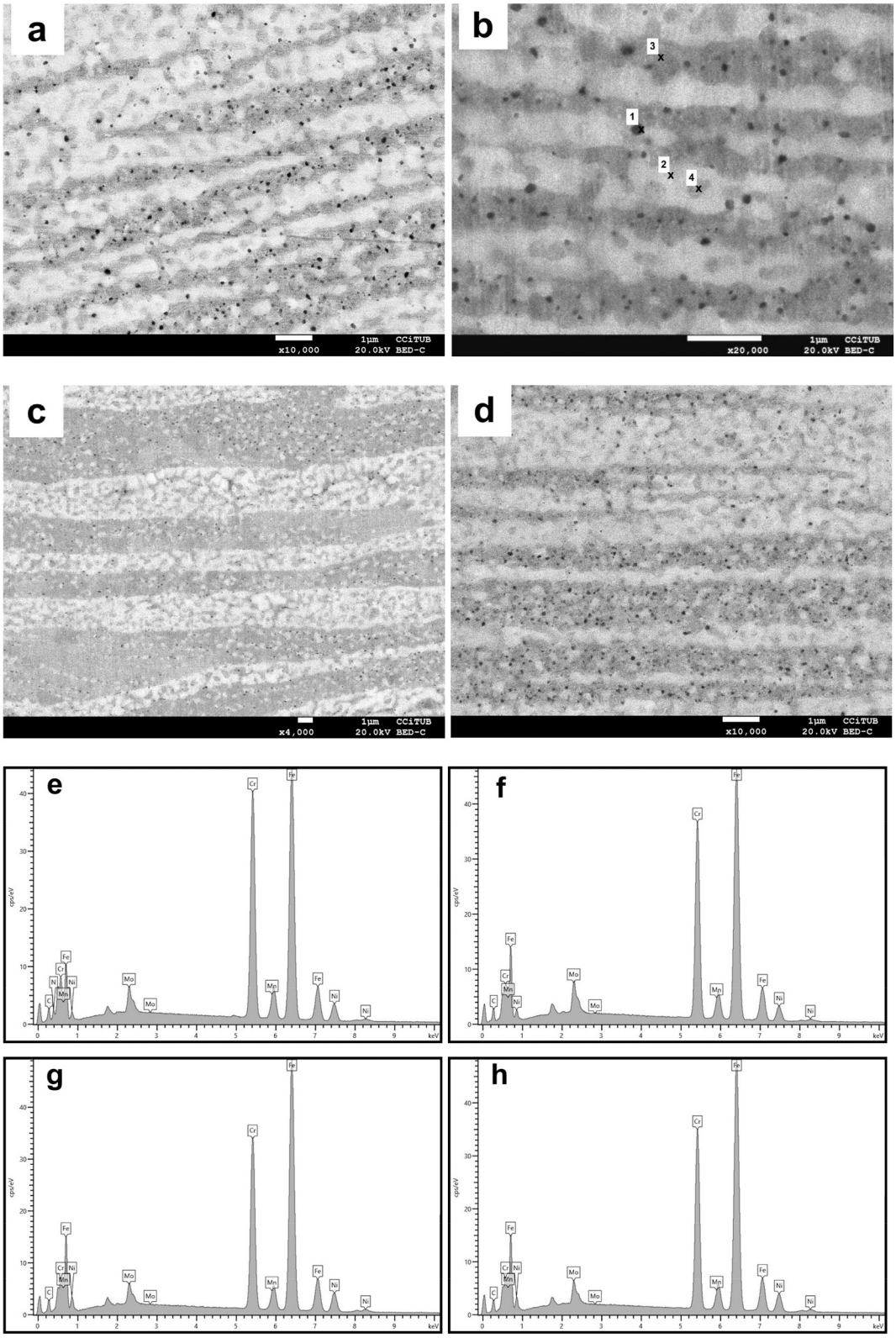

Fig. 4. BSE FE-SEM micrographs of SDSS samples (a) MST1 at the edge of the disc, (b) MST5 at the edge of the disc, (c) MST5 at the center of the disc, (d) MST10 at the edge of the disc and (e), (f), (g) and (h) EDS spectra of the pointed sites 1, 2, 3 and 4 in (b), respectively.

boundaries and triple points, presenting a coarse and irregular shape without any kind of pattern or morphology, enriched in Cr, as seen previously by STEM-EDS map, correspond to the tetragonal crystallographic structure of σ template/phase. The smaller grains, at the interface of austenite grains, around ~50 nm are perfectly matched to the trigonal crystallographic structure of chromium nitride (Cr_2N) template (crystallographic structures presented in Table 2 in Section 2). It is interesting to note that these grains are precipitating at the austenite grain boundaries and triple points. However, the indexation results, particularly of the supposedly σ phase (grains marked as 2, 3, 4 and 5 in

Table 4
EDS quantification for the sites marked in Fig. 3 (d) and Fig. 4 (b) for the samples MST0 and MST5, respectively.

	MST0				MST5			
Element	δ	γ	σ	Cr_2N	Point 1	Point 2	Point 3	Point 4
Cr	28.5	24.8	29.9	38.3	31.1	28.9	26.3	27.1
N	–	–	–	3.0	5.9	–	–	–
Mo	4.8	2.8	5.9	4.4	3.8	5.7	3.5	3.8
Ni	5.4	9.0	5.2	4.0	5.9	5.6	7.4	6.9

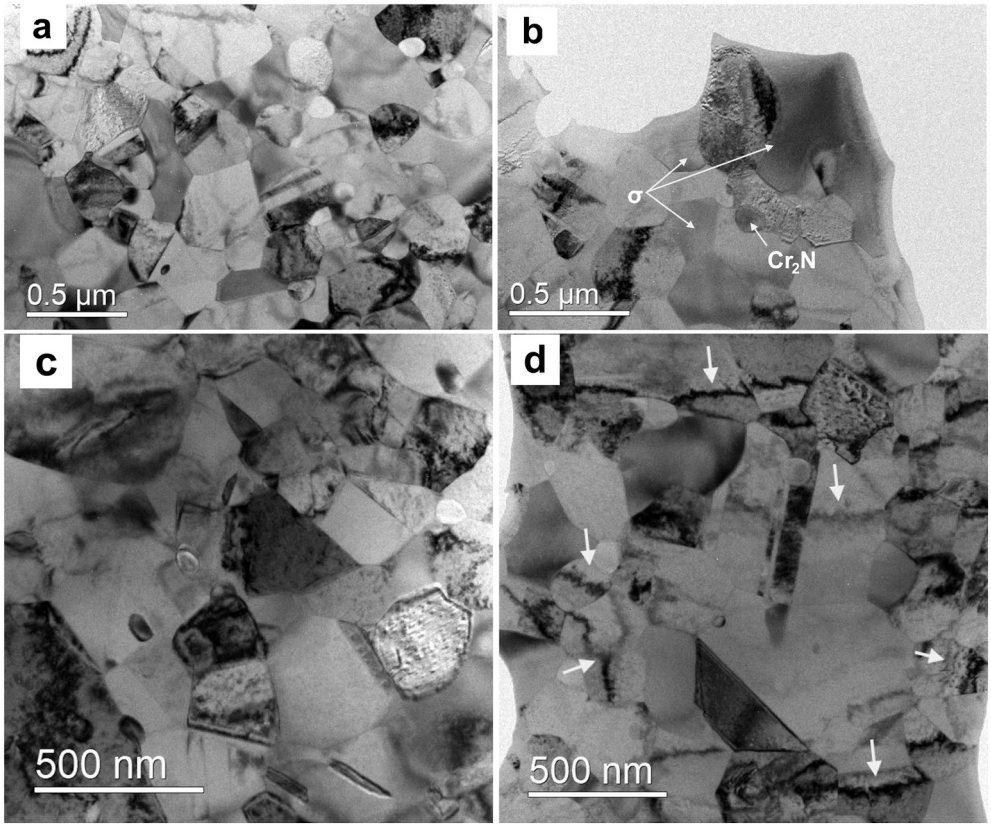

Fig. 5. BF-TEM images showing the microstructure of (a) and (b) MST1, (c) MST5 and (d) MST10 with grain size distribution slightly decreasing after each turn and precipitates after isothermal treatment.White arrows in (d) are showing accumulated disclocations forming dislocation barriers in the middle-end sized strained grains.

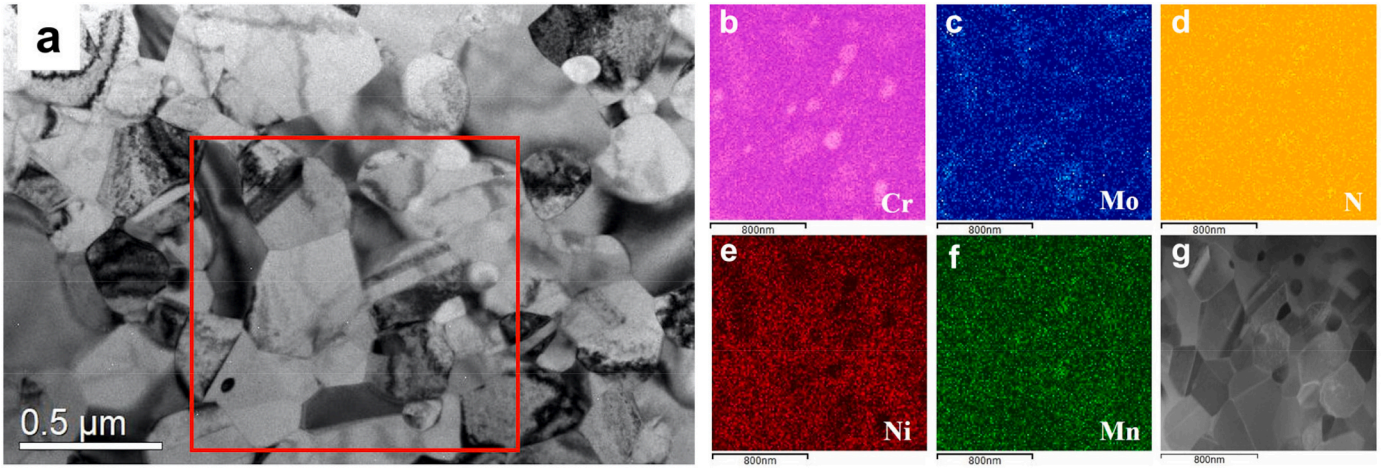

Fig. 6. (a) BF-TEM image of MST1 with red square marking the analyzed zone by SPED. (b)-(f) STEM-EDS element distribution of the selected area in (a) and (g) HAADF STEM image. (For interpretation of the references to colour in this figure legend, the reader is referred to the web version of this article.)

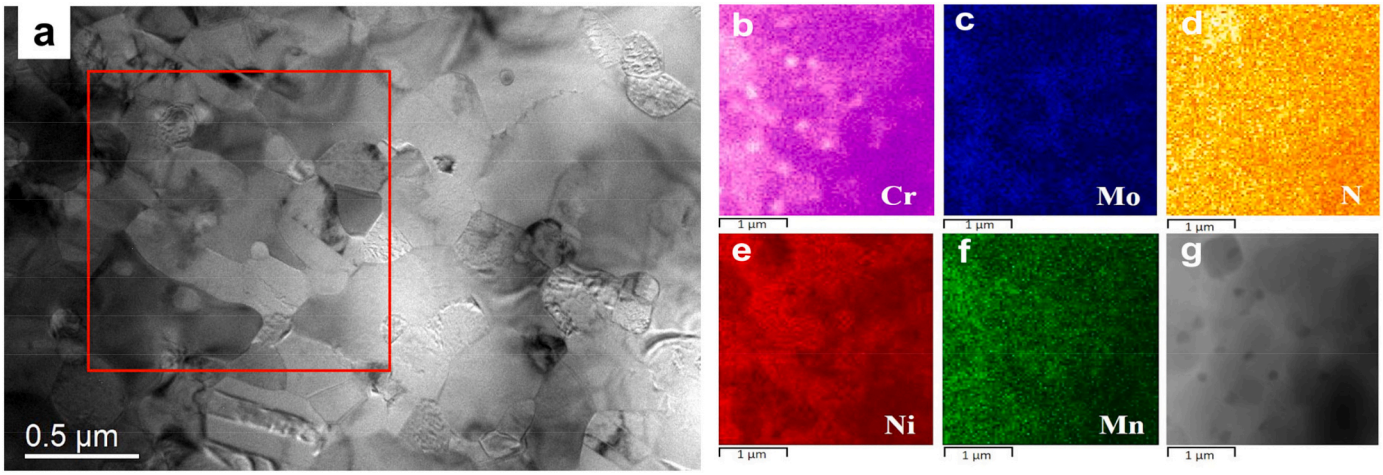

Fig. 7. (a) BF-TEM image of MST5 with red square marking the analyzed zone by SPED. (b)-(f) STEM-EDS element distribution of the selected area in (a) and (g) HAADF STEM image. (For interpretation of the references to colour in this figure legend, the reader is referred to the web version of this article.)

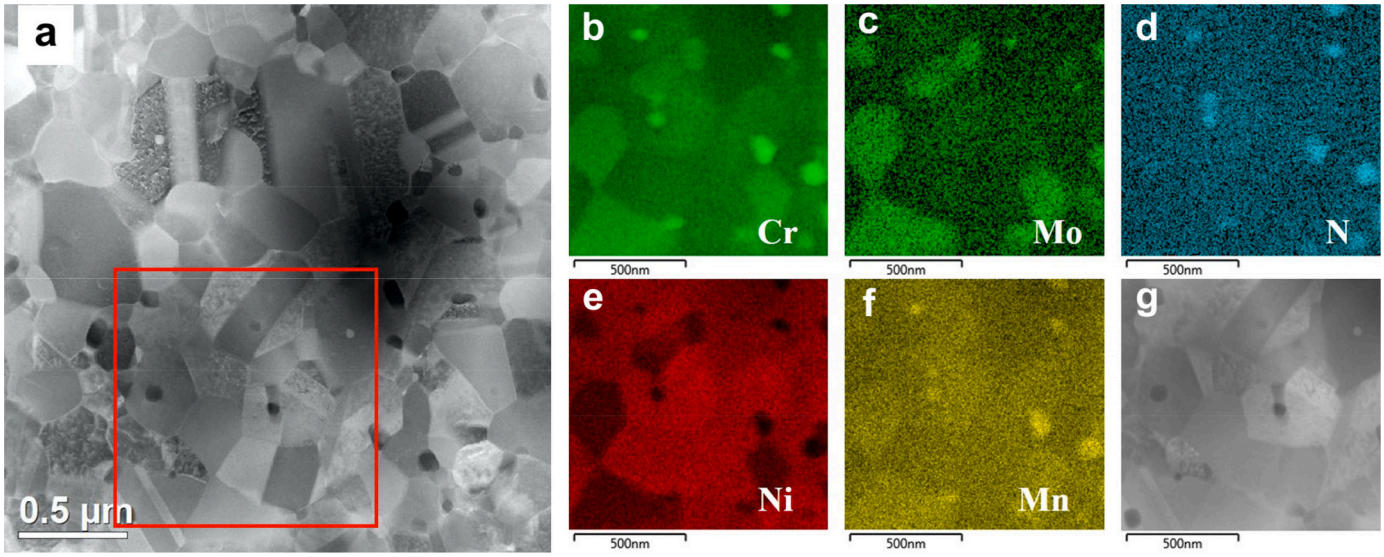

Fig. 8. (a) HAADF image of MST10 with red square marking the analyzed zone by SPED. (b)-(f) STEM-EDS element distribution of the selected area in (a) and (g) HAADF STEM image. (For interpretation of the references to colour in this figure legend, the reader is referred to the web version of this article.)

Fig. 9 (c)) present lower orientation reliability (OR). This could be both due to the different orientations of the crystals or due to the multiple phase indexation process. To reduce the chances of ambiguity, a smaller area, including a maximum of two different phases were indexed and this showed better indexation and reliability. Data can be found in the supplementary information. Further discussion about this issue is presented later in Section 4. The experimental diffraction patterns of the bigger grains, with characteristic twin boundaries inside, are perfectly matched to the simulated kinematic diffraction patterns of fcc-austenite template. Orientation map in the Z direction for austenite, σ and Cr_2N is shown in Fig. 9 (d). From the orientation map it can be seen that the brightest twin is perfectly matched to [110], as plotted by the inverse pole figure (IPF) coloring (fcc). The rest of the grains are randomly oriented.

3.4.3. Scanning precession electron diffraction analysis of MST5

Fig. 10 (a) and (b) show the virtual bright-field image of SPED data of the sample MST5 and the obtained indexed image, respectively. It is observed good indexation, except for the reliability drop at the grain boundaries at triple points. A superposition of grain boundaries is expected and hence it results in a poor reliability and a certain confusion while indexing (top left part of the scanned area). On the other hand, sigma phase in this sample is much brighter indicating high reliability in the indexed area (Fig. 10 (b)). In view of the growth of σ phase in this sample (all three phase map is shown in Fig. 10 (c)), it can be concluded that σ phase clearly appeared at the interface of differently oriented austenite grains (orientation map of all three phases is presented in Fig. 10 (d)). It should be mentioned that no grain could be matched to the template of bcc-ferrite. Although, the magnification is different from the sample MST1, Cr_2N are also around the size of the Cr_2N in MST1, ~50 nm or even larger. These were observed not only at the interfaces of austenite grain boundaries, but also attached to the σ phase, as observed in the phase map (Fig. 10. (c)). Almost all these Cr_2N present apparently at the same orientation preference, which is parallel to the [3030] (Fig. 10 (d)) as indicated by the IPF coloring of Cr_2N at the bottom of Fig. 10.

3.4.4. Scanning precession electron diffraction analysis of MST10

Fig. 11 (a) and (b) show the virtual brght-field and indexed images, respectively, of SPED data from a small scanned region of MST10

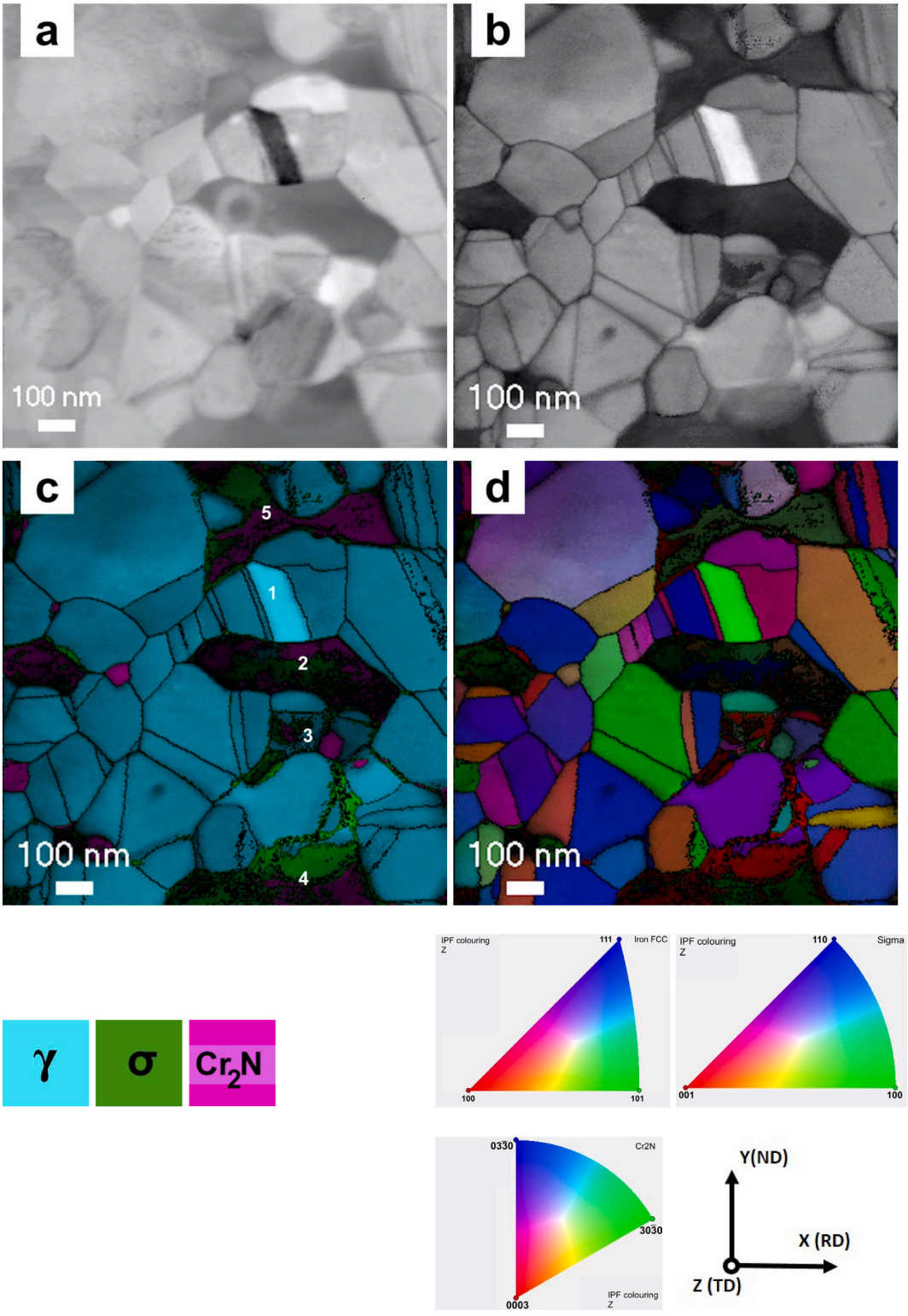

Fig. 9. SPED area for MST1 sample. (a) virtual bright field image, (b) indexed area image (c) phase map of all three phases (austenite - cyan, Cr_2N - purple and σ - green), (d) orientation map of all three phases in the Z direction. Numbers 2, 3,4 and 5 in phase map (c) are pointing to the low orientation realibitiy. Phase colour identification and directions considered for the samples and the IPF coloring for each phase are shown at the bottom. (For interpretation of the references to colour in this figure legend, the reader is referred to the web version of this article.)

sample. It contains similar grain size precipitated grains of Cr_2N (around 50 nm) and σ (around 600 nm) to the ones found in MST1 and MST5, as seen in the phase map in Fig. 11 (c). High brightening of the phase matched to σ phase template can be seen in the indexed image as well (Fig. 11 (b)) indicating high reliability. Most of the austenite grains indicate preferable orientation, parallel to the [111], as shown from the orientation map in Fig.11(d) and the IPF coloring for fcc austenite. Moreover, high orientation reliability of σ phase can be appreciated with random orientation (Fig. 11 (d)). Due to the smaller scanned area, there are less grains of Cr_2N, but some of them were not only placed at the

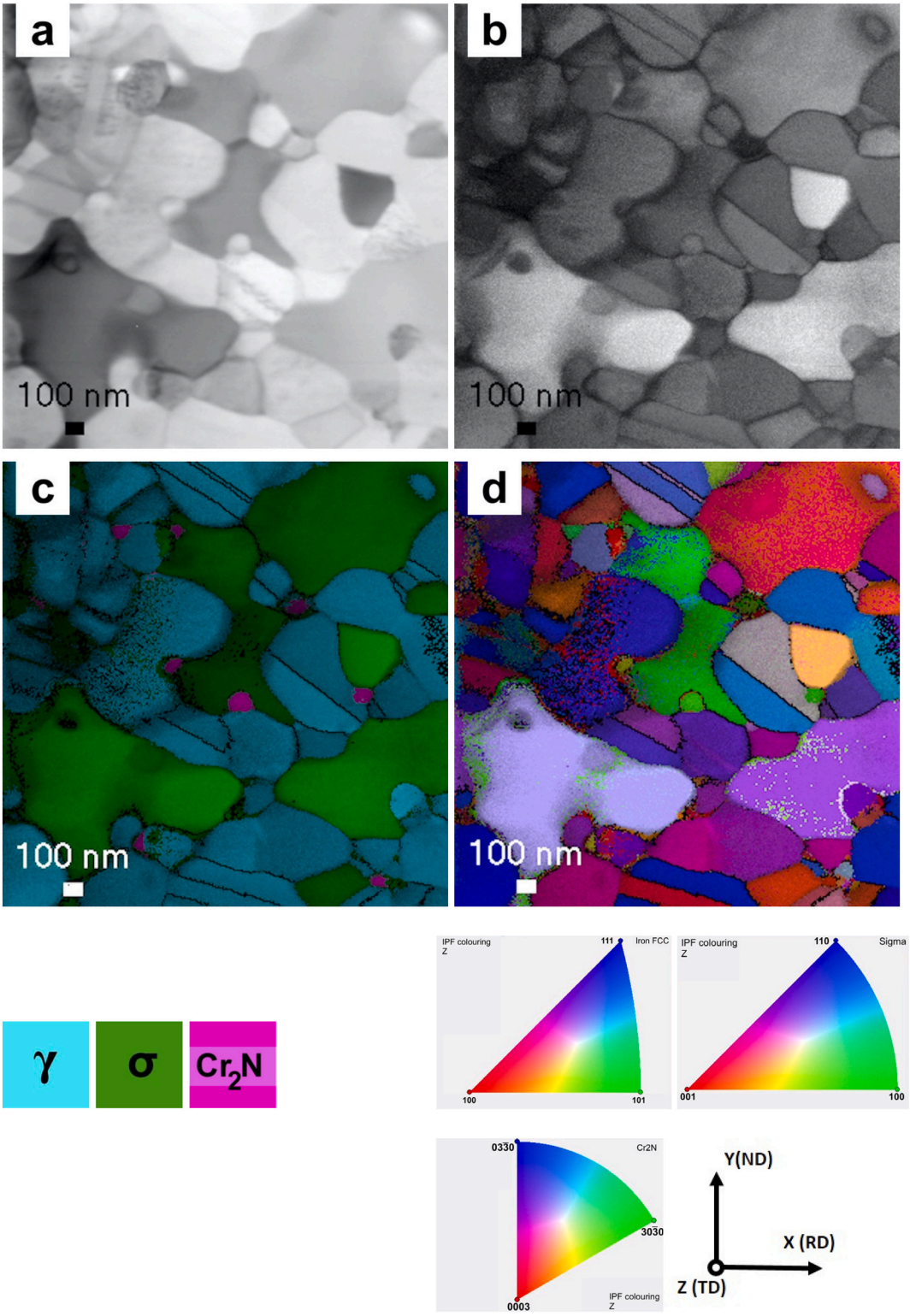

Fig. 10. SPED area for MST5 sample. (a) virtual bright field image, (b) indexed area image (c) phase map of all three phases (austenite - cyan, Cr_2N - purple and σ - green), (d) orientation map of all three phases in the Z direction. Phase colour identification and directions considered for the samples and the IPF coloring for each phase are shown at the bottom. (For interpretation of the references to colour in this figure legend, the reader is referred to the web version of this article.)

austenite grain boundaries but also at the twin boundary. Particularly, one of them, marked as 1 in Fig. 11 (c) is found in between the twin boundary of the austenite grain. Such nucleation site is favorable due to the higher internal energy.

3.5. Hardness evolution before and after heat treamtnet

Mechanical properties of the severely deformed samples were analyzed through microhardness tests. The evolution of the hardness of the non-processed and HPT processed samples has been studied before and after the isothermal treatment emphasizing mainly the increase of

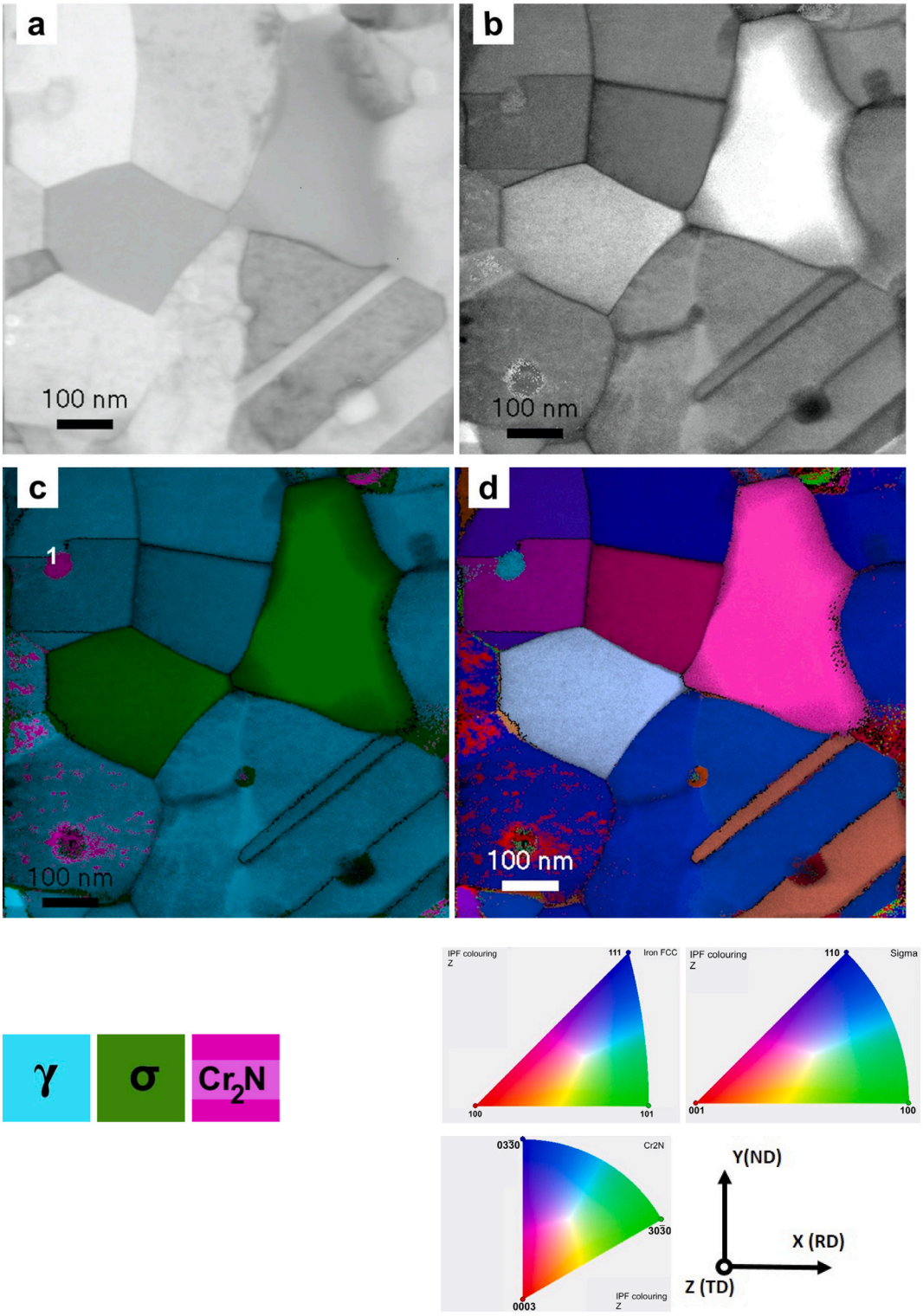

Fig. 11. SPED area for MST10 sample. (a) virtual bright field image, (b) indexed area image (c) phase map of all three phases (austenite - cyan, Cr_2N - purple and σ - green), (d) orientation map of all three phases in the Z direction. Phase colour identification and directions considered for the samples and the IPF coloring for each phase are shown at the bottom. Number 1 in phase map (a) is pointing to Cr_2N precipitate at twin boundary site. (For interpretation of the references to colour in this figure legend, the reader is referred to the web version of this article.)

the values after significant increase in σ precipitation. In Fig. 12, the graphical representation of the hardness values obtained through the diameter of the samples before the isothermal treatment (dashed line) and after the isthermal treatment (continued line) are presented. The difference in hardness between the annealed sample, without HPT deformation applied (MS0), 283 ± 12 HV0.1 and the MS10 sample, 621 ± 17 HV0.1 is large. Hardness at the center ($r = 0$) of the deformed samples decreases slightly. However, less difference along the diameter is observed when HPT turns (induced strain), are increased. There is almost 3.5% of difference between 5 and 10 HPT turns, from 598 ± 37

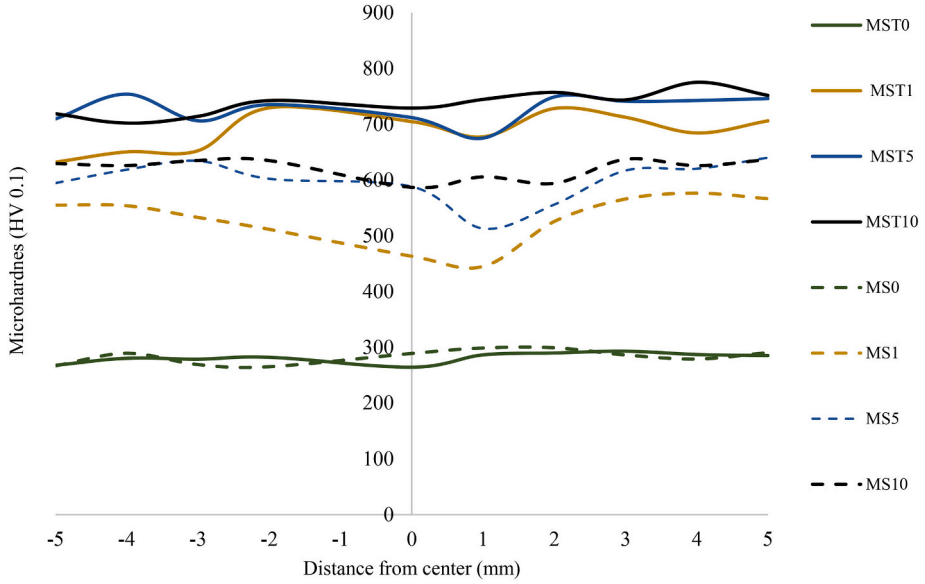

Fig. 12. Microhardness (HV 0.1) vs distance (mm) graphical representation and hardness values distribution before (dashed line) and after (continued line) isothermal treatment applied to the HPT along the diameter of the disc samples.

HV0.1 to 621 ± 17 HV0.1. Moreover, around 55% of hardness increase has been observed from the non-processed sample (MS0) to the sample processed with the maximum HPT turns (MS10). As happens with other SPD processing, the highest increase in hardness occurs after the first turn in HPT in which hardness value increases by 46%. The hardness distribution of the samples after the isothermal treatment is also shown. The sample without deformation applied (MST0) shows similar values as the sample without isothermal treatment, indicating that small amount of σ phase has precipitated. However, the strengthening of the material is higher for all three samples deformed by HPT and annealed afterwards. Indeed, very similar values are achieved for all of them, 688 ± 32 HV0.1, 727 ± 24 HV0.1 and 738 ± 21 HV0.1 for MST1, MST5 and MST10, respectively. It is considered that due to the homogenously distributed σ phase in the deformed samples (Fig. 4), the mechanical strength of the material is increased in comparison to the samples without precipitates.

4. Discussion

The main objective of this section is to discuss the impact of HPT on the microstructural evolution of samples isothermally treated afterwards. The precipitation of the intermetallic phases before and after the SPD process was different and so are the mechanical properties of the material. Research on duplex stainless steels, severely deformed by hydrostatic extrusion (HE), which is a powerful grain size refining process, has been carried out by P. Maj et al. [41] with a similar aim to enhance precipitation process after annealing. With the comparatively smaller equivalent strain obtained after HE ($\varepsilon = 3.8$), phase transformation of austenite phase into deformation induced martensite ($\gamma \rightarrow \alpha'$) was observed. This result was also found by Taveras et al. after cold rolling [42]. This transformation additionally enhances the mechanical properties of the material. However, in the current experimental results, no phase transformation was seen. Secondary phase precipitation was observed after an isothermal treatment and the hardness was almost twice as that of the sampleon which less severe technique is applied. It is to be taken into account that the grade of duplex stainless steel in the current study is UNS3 2750.

To discuss the influence of the deformation induced in the samples on the precipitation of the intermetallic phases, it is relevant to consider the same isothermal treatment before and after HPT deformation process.

4.1. Before HPT deformation

According to the Thermo-calc calculations, from the phase equilibrium diagram in Fig. 2, precipitation of the σ phase can occur up to ~980 °C. Therefore, at 830 °C (the temperature selected for the experiments) 33 wt% of σ is expected. Observing the micrographs of the experimental treatment (Fig. 3), disperse σ phase is detected occasionally (and confirmed by EDS, Fig. 3 (e)). Hence, there is still a majority of the delta ferrite phase and σ has not yet replaced it completely. In addition, the treatment carried out has been at an isothermal temperature for a relatively short time, unlike the phases presented in the diagram that would correspond to continuous cooling treatment and longer time of aging. On the other hand, it is worth mentioning that no carbides were detected by EDS in this experimental analysis which is in accordance with the equilibrium diagram obtained previously and with reports in the literature for the same material [20,43,44].

The morphology of the precipitated σ phase in stainless steels is described in the literature in four types [45,46]. For instance, it is mostly found at γ/δ and γ/γ grain boundaries, triple points, corner sites and also inside the ferrite grains with cellular precipitation morphology. Grain boundaries are preferable sites for precipitation due to the higher interfacial energy. At these points blocky σ morphology is mostly observed. The same aspect was seen in the current experiments (Fig. 3). These points are also rich in Cr-containing regions which, as a consequence to the precipitation, local low Cr regions are formed. There are several authors who consider the region near the σ phase as a new phase, and they named it secondary austenite phase, γ_2. This region is depleted in Cr and richer in Ni when compared to the prior austenite phase composition, γ. Secondary austenite, therefore, is described as a result of the transformation of δ-ferrite to σ, theoretically known as an eutectoid reaction ($\delta \rightarrow \sigma + \gamma_2$) [39,47–50]. Here, it is relevant to clarify the concept of eutectoid transformation. The reaction consists of the transformation of a stable solid phase into two stable solid phases at constant temperature, as described in the classical physical metallurgy books from the Fe-Fe_3C diagrams and handbooks [51]. In the case of the σ phase precipitation, first of all, the morphology of the intermetallic σ phase changes depending on the site it precipitates in the same sample and under the same treatment, unlike the lamellar morphology of perlite in the classic eutectoid reaction. Furthermore, precipitation occurs in a range of temperatures and depending on this, the morphology of the phase is different [45]. This can be block-like, as in the case of the

current experiments, when aging temperatures are not too high and precipitation occurs at grain boundaries (Fig. 3). It can happen as a cellular precipitation at lower temperatures and longer time of precipitation, or as seen in the current deformed samples, when microstructure is highly strained and with high angle grain boundaries in abundance (Fig. 4). Also, the mole fraction of the phase varies depending on the temperature and aging time. However, a typical eutectoid reaction occurs at a constant temperature. It is a solid-state invariant reaction occurring by a long range discontinuous mass transport and thermally activated heterogeneous transformation involving moving reaction boundaries and phase separation. Precipitation reactions differ from invariant transformations in the fact that the former involve the formation of a new second phase within a matrix that has the same crystal structure as the parent phase. In contrast, all the reaction products from invariant transformations have a different crystal structure than that of the parent phase as stated in the ASM handbook for microstructures and microanalyses of Metals [52]. In addition, σ precipitation at corner sites tends to consume the δ-ferrite completely when left for long enough aging time. In these experiments, the isothermal treatment at 830 °C for a relatively short time, was enough for the σ nucleation, but it was not enough for its expansion and complete consumption of the ferrite phase. The mechanism of formation of σ phase in this study was mainly at γ/δ and γ/γ grain boundaries with a blocky shape without observing the total exhaustion of ferrite, mainly because too short time of aging was allowed. Most importantly, there is no sign of secondary austenite precipitation. Moreover, no eutectoid transformation can be concluded for the samples observed previously to HPT deformation due to the mentioned above considerations.

Chromium nitrides, on the other hand, precipitate before σ phase at the grain boundaries of δ/δ γ/δ and triple points. Precipitation of Cr_2N prevail, due to the high percentage of N in the composition of the steel. As can be seen in all micrographs of Fig. 3, a line contour of Cr_2N is formed around the austenite/ferrite, austenite/austenite and ferrite/ferrite interfaces. The nucleation of these Cr_2N precipitates occurs in the center of the ferrite grain diffusion path, as a depletion of Cr, N and Mo from inner ferrite is observed, which is in agreement with Warren et al. [53] and Bobadilla et al. [54]. The ferritic phase is characterized by high diffusion and low solubility in nitrogen. Therefore, the precipitation of chromium nitrides is favored when rapid cooling is performed. Additionally, as seen in the experimental results and found by previous research [6], chromium nitrides are preferable nucleation sites for χ phase precipitation, which then tend to disappear if σ phase is precipitating for longer time. Thus, Cr_2N are also considered as σ phase nucleation sites afterwards. This precipitation, according to several authors, in superduplex, hyperduplex and lean stainless steels, is accompanied by the formation of "secondary austenite", as well [20,55,57]. However, the depleted zone near σ and/or Cr_2N precipitation should be considered as a consequence of the diffusion process during the formation of these precipitates.

4.2. After HPT deformation

The heterogeneous deformation produced by HPT process and other SPD methods in dual phase stainless steels, containing both ferrite and austenite phases, has been studied in the last decade [58–62]. It has been seen that the differences between austenite (fcc) and ferrite (bcc), from the crystallographic point of view, are enough to promote different deformation mechanisms during the initial stages of deformation. Due to the high strain induced in the samples, the deformation strain is transferred almost equally from both phases at least at 5 and 10 turns HPT. Thus, no significant differences concerning precipitate grain size and morphology as well as hardness were found between the turns as observed from the SPED orientantion and phase mapping and hardness values obtained for each sample.

It is well known that SPD enhances the precipitation rate after a subsequent annealing treatment [41–55,57–63]. The already strained microstructure in which dislocation density is increased and twin boundaries are present, high concentration of vacancies is also generated. Thus, when combined with temperature, microstructure tends to rearrange atomically. Dislocation-precipitate interaction, grain boundary-precipitate interaction, dislocation slip, and atomic diffusion are the possible interactions that can occur after precipitation in the SPD microstructure [64]. Due to the presence of multiple defects, fast diffusion path for solute atoms in the matrix takes place when a dislocation line is found as suggested by Kuzmina et al. [65]. Thereby, the rapid diffusion assists the growth of intermetallic precipitates. From the SEM (Fig. 4), no ferrite was detected and therefore σ within the austenite phase and small dark phases of Cr_2N were only seen. The faster diffusion of Cr and N promoted higher concentration of nitride nucleation, subsequently there are more nucleation sites for sigma. Severe local shear may bring two well-separated precipitates closer together and promote their coalescence as well [66]. Hence, the close phases at the grain boundaries may lead to an overlapped bigger phase, as seen in the previous images from SPED data, where σ showed coarse grains (Figs. 9, 10, 11). The grain size decrease after HPT promotes the appearance of high-angle grain boundaries which are the most favorable nucleation sites. These are considered more energetically active. Eventually, the precipitation rate accelerates at increased high-angle grain boundaries. Therefore, the generated vacancies during the HPT and the abundance of high-angle boundaries that increase by HPT turns, promote faster diffusion and the σ precipitation has been favored and homogenously distributed in the deformed microstructure. As the result showed, the highest hardness values were obtained after precipitation happened. Herein, the strength increase is attributed to the strain aging related phenomena [67]. The interaction of precipitates with dislocations hinder the dislocation movement and the homogenous distribution of sigma in the microstructure probably lead to the increase of hardness in the material. This is also found by P. Maj et al. [41] within much lower induced strain in 2205 duplex stainless steel.

Local diffraction patterns were useful as a complementary information to see the precipitate interaction with the strained matrix at nanoscale. These diffraction patterns contain crystallographic and orientation information about the structure and are frequently obtained through EBSD in a SEM, based on the Kikuchi patterns. However, when a little distortion is present in the microstructure, they become more sensitive and are difficult to obtain [29]. For this reason, TEM and SPED technique are required as donein the present study. Using the information from STEM-EDS analysis, the identification of phases and the orientation characterization of these phases were taken forward by SPED in an automated scanning mode and it was possible to scan over a larger area, covering more pixels on each grain, facilitating the analysis. Some limitations of the Index software by Nanomegas, for the phase indetification, are related to its lower reliability when more than three templates are given as inputs. Thus, along with the indexation, manual intervention is considered to assure the phase identification and check the template/experimental pattern matching. A low reliability indexation of the phases, particularly the ones assigned to σ has been observed in MST1. This could also be correlated to the on-going precipitation process of σ into the ferrite phase. In addition, σ phase has not grown at all in that area, and due to the diffusion of the elements in the near zone, low indexation realibility is obtained. In comparison to MST5 and MST10, σ phase is much more expanded, found at triple points of austenite/nitride/austenite. At the same time, Cr_2N has been observed as probable nucleation site of σ, especially in MST5. From the orientation maps obtained by SPED, it was observed that sigma and Cr_2N show different orientations and are randomly distributed.

5. Conclusions

HPT severely deformed UNS S32750 superduplex stainless steel with a post-isothermal treatment, showed enhanced precipitation of intermetallic secondary phases in comparison to the unprocessed

(undeformed) samples microstructure. σ and Cr_2N are the main precipitates found in the microstructure after 1, 5 and 10 turns of HPT, presenting similar tendency and homogeneous distribution as well as size and morphology in all the three samples. The high deformation induced in the microstructure, even after 1 turn HPT required high resolution microscopy techniques. Scanning precession electron diffraction technique was used to confirm and finally determine that random orientation distribution of precipitates was observed. High dislocation density and vacancies within induced strained microstructure after HPT process led to the interaction of precipitates and dislocations, resulting in a more strengthened microstructure, attributed to the strain aging phenomenon. σ phase formed mainly, but not exclusively, at the triple point of austenite/nitride/austenite and austenite/austenite/austenite. The results confirmed that Cr_2N seem to be the preferred nucleation sites for σ phase at higher deformation strain. Finally, precipitation is not considered as an eutectoid reaction but as an invariant transformation, where σ is a product from a solid-state parent phase with different crystal structure.

Data availability

The raw/processed data required to reproduce these findings cannot be shared at this time as the data also forms part of an ongoing study.

Declaration of Competing Interest

The authors declare that they have no known competing financial interests or personal relationships that could have appeared to influence the work reported in this paper.

Acknowledgments

The research leading to these results has received funding from the European Union Horizon 2020 research and innovation program under grant agreement No. 823717 – ESTEEM3. The 2100F was financed with support of NORTEM (Grant 197405) within the program INFRASTRUCTURE of the Research Council of Norway (RCN).

Appendix A. Supplementary data

Supplementary data to this article can be found online at https://doi.org/10.1016/j.matchar.2021.111639.

References

[1] G. Chail, P. Kangas, Super and hyper duplex stainless steels: structures, properties and applications, Proc. Struct. Integr. 2 (2016) 1755–1762.
[2] X. Liu, W. Lu, X. Zhang, Reconstructing the decomposed ferrite phase to achieve toughness regeneration in a duplex stainless steel, Acta Mater. 183 (2020) 51–63.
[3] C.C. Hsieh, W. Wu, Overview of intermetallic sigma (σ) phase precipitation in stainless steels, International Scholarly Research Notices 2012 (2012).
[4] D.M.E. Villanueva, F.C.P. Junior, R.L. Plaut, A.F. Padilha, Comparative study on sigma phase precipitation of three types of stainless steels: austenitic, superferritic and duplex, Mater. Sci. Technol. 22 (9) (Sep. 2006) 1098–1104.
[5] H. Sieurin, R. Sandström, Sigma phase precipitation in duplex stainless steel 2205, Mater. Sci. Eng. A 444 (1–2) (2007) 271–276.
[6] N. Llorca-Isern, H. López-Luque, I. López-Jiménez, M.V. Biezma, Identification of sigma and chi phases in duplex stainless steels, Mater. Charact. 112 (Feb. 2016) 20–29.
[7] S. Atamert, J.E. King, Sigma-phase formation and its prevention in duplex stainless steels, J. Mater. Sci. Lett. 12 (14) (1993) 1144–1147.
[8] J.O. Nilsson, P. Liu, Aging at 400-600°C of submerged arc welds of 22Cr-3Mo-8Ni duplex stainless steel and its effect on toughness and microstructure, Mater. Sci. Technol. (United Kingdom) 7 (9) (Sep. 1991) 853–862.
[9] M. Hättestrand, P. Larsson, G. Chai, J.-O. Nilsson, J. Odqvist, Study of decomposition of ferrite in a duplex stainless steel cold worked and aged at 450–500°C, Mater. Sci. Eng. A 499 (1–2) (Jan. 2009) 489–492.
[10] H.M. Ezuber, A. El-Houd, F. El-Shawesh, Effects of sigma phase precipitation on seawater pitting of duplex stainless steel, Desalination 207 (1–3) (2007) 268–275.
[11] D.Y. Kobayashi, S. Wolynec, Evaluation of the low corrosion resistant phase formed during the sigma phase precipitation in duplex stainless steels, Mater. Res. 2 (4) (1999) 239–247.
[12] J.-O. Nilsson, Super duplex stainless steels, Mater. Sci. Technol. 8 (8) (Aug. 1992) 685–700.
[13] J.O. Nilsson, A. Wilson, Influence of isothermal phase transformations on toughness and pitting corrosion of super duplex stainless steel SAF 2507, Mater. Sci. Technol. 9 (7) (1993) 545–554.
[14] B.M. Efros, V.P. Pilyugin, A.M. Patselov, Y.Y. Beygelzimer, N.B. Efros, Ultrafine Grained Materials II, 2002.
[15] S.V. Dobatkin, J. Zrník, I. Mamuzić, Nanostructures by severe plastic deformation of steels: advantages and problems, Metalurgija 45 (4) (2006) 313–321.
[16] X.Z. Liang, M.F. Dodge, W. Liang, H.B. Dong, Precipitation of chromium nitride nano-rods on lamellar carbides along austenite-ferrite boundaries in super duplex stainless steel, Scripta Materialia 127 (2017) 45–48. Complete.
[17] V. Hosseini, L. Karlsson, S. Wessman, N. Fuertes, Effect of sigma phase morphology on the degradation of properties in a super duplex stainless steel, Materials (Basel). 11 (6) (Jun. 2018).
[18] M. Pohl, O. Storz, T. Glogowski, Effect of sigma-phase morphology on the properties of duplex stainless steels, Microscopy and Microanalysis 11 (S02) (2005) 230–231.
[19] D.V. Bayão, G.L. de Faria, E.C.M. Arthuso, J.R. de Oliveira Júnior, S.N. da Silva, I. P. Pinheiro, Estudio cinético da precipitação de fase sigma em um aço inoxidável duplex UNS S31803 envelhecido isotermicamente a 750°C, 800°C E 850°C, 2020 no. October, pp. 2445–2458.
[20] J.Y. Maetz, T. Douillard, S. Cazottes, C. Verdu, X. Kléber, M23C6 carbides and Cr2N nitrides in aged duplex stainless steel: A SEM, TEM and FIB tomography investigation, Micron 84 (2016) 43–53.
[21] K.M. Lee, H. Cho, D.C. Choi, Effect of isothermal treatment of SAF 2205 duplex stainless steel on migration of δ/γ interface boundary and growth of austenite, J. Alloys Compd. 285 (1–2) (1999) 156–161. Complete.
[22] R.Z. Valiev, Y. Estrin, Z. Horita, T.G. Langdon, M.J. Zehetbauer, Y.T. Zhu, Producing bulk ultrafine-grained materials by severe plastic deformation, JOM 58 (4) (Apr-2006) 33–39.
[23] A. Azushima, et al., Severe plastic deformation (SPD) processes for metals, CIRP Ann. - Manuf. Technol. 57 (2) (2008) 716–735.
[24] R.Z. Valiev, R.K. Islamgaliev, I.V. Alexandrov, Bulk nanostructured materials from severe plastic deformation, Prog. Mater. Sci. 45 (2) (2000) 103–189.
[25] Y. Maehara, Superplasticity of delta-Ferrite/austenite duplex stainless steels, Trans. Iron Steel Inst. Japan 25 (1) (1985) 69–76.
[26] R. Vincent, P.A. Midgley, Double conical beam-rocking system for measurement of integrated electron diffraction intensities, Ultramicroscopy 53 (3) (Mar. 1994) 271–282.
[27] E.F. Rauch, J. Portillo, S. Nicolopoulos, D. Bultreys, S. Rouvimov, P. Moeck, Automated nanocrystal orientation and phase mapping in the transmission electron microscope on the basis of precession electron diffraction, Z. Krist. 225 (2–3) (2010) 103–109.
[28] J.O. Andersson, T. Helander, L. Höglund, P. Shi, B. Sundman, Thermo-Calc & DICTRA, computational tools for materials science, Calphad Comput. Coupl. Phase Diagrams Thermochem. 26 (2) (Jun. 2002) 273–312.
[29] E.F. Rauch, L. Dupuy, Rapid spot diffraction patterns identification through template matching, Arch. Metall. Mater. 50 (1) (2005) 87–99.
[30] E. Parthé, et al., Crystal chemical characterization of inorganic structure types, in: TYPIX — Standardized Data and Crystal Chemical Characterization of Inorganic Structure Types, Springer Berlin Heidelberg, 1993, pp. 41–260.
[31] E.F. Rauch, M. Véron, Automated crystal orientation and phase mapping in TEM, Mater. Charact. 98 (2014) 1–9.
[32] H.L. Yakel, Atom distributions in sigma phases. I. Fe and Cr atom distributions in a binary sigma phase equilibrated at 1063, 1013 and 923 K, Acta Crystallogr. Sect. B 39 (1) (Feb. 1983) 20–28.
[33] E.F. Rauch, M. Veron, Coupled microstructural observations and local texture measurements with an automated crystallographic orientation mapping tool attached to a tem, Mater. Werkst. 36 (10) (2005) 552–556.
[34] M.V. Degtyarev, T.I. Chashchukhina, L.M. Voronova, A.M. Patselov, V.P. Pilyugin, Influence of the relaxation processes on the structure formation in pure metals and alloys under high-pressure torsion, Acta Mater. 55 (18) (2007) 6039–6050.
[35] A.P. Zhilyaev, T.G. Langdon, Using high-pressure torsion for metal processing: Fundamentals and applications, Prog. Mater. Sci. 53 (6) (Aug. 2008) 893–979.
[36] I. Calliari, M. Breda, C. Gennari, L. Pezzato, M. Pellizzari, A. Zambon, Investigation on solid-state phase transformations in a 2510 duplex stainless steel grade, Metals (Basel). 10 (7) (Jul. 2020) 1–12.
[37] N. Sathirachinda, R. Pettersson, S. Wessman, U. Kivisäkk, J. Pan, Scanning Kelvin probe force microscopy study of chromium nitrides in 2507 super duplex stainless steel - Implications and limitations, Electrochim. Acta 56 (4) (2011) 1792–1798.
[38] J.W. Elmer, T.A. Palmer, E.D. Specht, Direct observations of sigma phase formation in duplex stainless steels using In-situ synchrotron X-ray diffraction, Metall. Mater. Trans. A Phys. Metall. Mater. Sci. 38 (3) (Mar. 2007) 464–475.
[39] M. Martins, L.C. Casteletti, Sigma phase morphologies in cast and aged super duplex stainless steel, Mater. Charact. 60 (8) (2009) 792–795.
[40] J.M. Shockley, D.J. Horton, K.J. Wahl, Effect of aging of 2507 super duplex stainless steel on sliding tribocorrosion in chloride solution, Wear 380–381 (2017) 251–259.
[41] P. Maj, B. Adamczyk-Cieslak, J. Nowicki, J. Mizera, M. Kulczyk, Precipitation and mechanical properties of UNS 2205 duplex steel subjected to hydrostatic extrusion after heat treatment, Mater. Sci. Eng. A 734 (March) (2018) 85–92.
[42] S.S.M. Tavares, M.R. da Silva, J.M. Pardal, H.F.G. Abreu, A.M. Gomes, Microstructural changes produced by plastic deformation in the UNS S31803 duplex stainless steel, J. Mater. Process. Technol. 180 (1–3) (Dec. 2006) 318–322.

[43] N. Sathirachinda, R. Pettersson, S. Wessman, J. Pan, Study of nobility of chromium nitrides in isothermally aged duplex stainless steels by using SKPFM and SEM/EDS, Corros. Sci. 52 (1) (Jan. 2010) 179–186.
[44] A.J. Ramirez, J.C. Lippold, S.D. Brandi, The relationship between chromium nitride and secondary austenite precipitation in duplex stainless steels, Metall. Mater. Trans. A Phys. Metall. Mater. Sci. 34 A (8) (2003) 1575–1597.
[45] C.C. Hsieh, D.Y. Lin, T.C. Chang, Microstructural evolution during the δ/σ/γ phase transformation of the SUS 309LSi stainless steel after aging under various nitrogen atmospheric ratios, Mater. Sci. Eng. A 475 (1–2) (2008) 128–135.
[46] M.V. Biezma, U. Martin, P. Linhardt, J. Ress, C. Rodríguez, D.M. Bastidas, Non-destructive techniques for the detection of sigma phase in duplex stainless steel: a comprehensive review, Eng. Fail. Anal. 122 (Jan. 2021) 105227.
[47] M. Pohl, O. Storz, T. Glogowski, Effect of intermetallic precipitations on the properties of duplex stainless steel, Mater. Charact. 58 (1) (2007) 65–71.
[48] K.N. Adhe, V. Kain, K. Madangopal, H.S. Gadiyar, Influence of sigma-phase formation on the localized corrosion behavior of a duplex stainless steel, J. Mater. Eng. Perform. 5 (4) (Aug. 1996) 500–506.
[49] C.-S. Huang, C.-C. Shih, Effects of nitrogen and high temperature aging on σ phase precipitation of duplex stainless steel, Mater. Sci. Eng. A 402 (1–2) (Aug. 2005) 66–75.
[50] R.O. Sousa, P. Lacerda, P.J. Ferreira, L.M.M. Ribeiro, On the precipitation of sigma and chi phases in a cast super duplex stainless steel, Metall. Mater. Trans. A 50 (10) (2019) 4758–4778.
[51] H. Baker, H. Okamoto, ASM Handbooks Volume 3 - Alloy Phase Diagrams, ASM International, Materials Park, 1992.
[52] T. Materials, ASM Handbook, Volume 9, Metallography and Microstructures vol. 9, 2004.
[53] A.D. Warren, I.J. Griffiths, P.E.J. Flewitt, Precipitation within localised chromium-enriched regions in a Type 316H austenitic stainless steel, J. Mater. Sci. 53 (8) (2018) 6183–6197.
[54] M. Bobadilla, A. Tschiptschin, On the nitrogen diffusion in a duplex stainless steel, Mater. Res. 18 (2) (Oct. 2015) 390–394.
[55] F. Tehovnik, B.Š. Batič, F. Vode, S. Malej, J. Burja, Nitrides and carbides in 2101 lean duplex stainless steel, Mater. Tehnol. 52 (6) (2018) 821–826.
[57] V.A. Hosseini, L. Karlsson, C. Örnek, P. Reccagni, S. Wessman, D. Engelberg, Microstructure and functionality of a uniquely graded super duplex stainless steel designed by a novel arc heat treatment method, Mater. Charact. 139 (May 2018) 390–400.
[58] Y. Huang, M. Kawasaki, T.G. Langdon, An investigation of flow patterns and hardness distributions using different anvil alignments in high-pressure torsion, J. Mater. Sci. 48 (13) (2013) 4533–4542.
[59] Y. Cao, Y.B. Wang, X.H. An, X.Z. Liao, M. Kawasaki, S.P. Ringer, T.G. Langdon, Y. T. Zhu, Concurrent microstructural evolution of ferrite and austenite in a duplex stainless steel processed by high-pressure torsion, Acta Mater. 63 (2014) 16–29.
[60] K.T. Schwarz, K.S. Kormout, R. Pippan, A. Hohenwarter, Impact of severe plastic deformation on microstructure and fracture toughness evolution of a duplex-steel, Mater. Sci. Eng. A 703 (May) (2017) 173–179.
[61] W. Jiang, et al., On the heterogeneity of local shear strain induced by high-pressure torsion, Adv. Eng. Mater. 22 (1) (Jan. 2020) 1900477.
[62] P. Maj, B. Adamczyk-Cieślak, J. Mizera, W. Pachla, K.J. Kurzydłowski, Microstructure and mechanical properties of duplex stainless steel subjected to hydrostatic extrusion, Mater. Charact. 93 (Jul. 2014) 110–118.
[63] Y. Cao, S. Ni, X. Liao, M. Song, Y. Zhu, Structural evolutions of metallic materials processed by severe plastic deformation, Mater. Sci. Eng. R. Rep. 133 (May) (Nov. 2018) 1–59.
[64] R.Z. Valiev, V.Y. Gertsman, O.A. Kaibyshev, Non-equilibrium state and recovery of grain boundary structure. II. Energetic Analysis, Phys. Status Solidi 78 (1) (1983) 177–186.
[65] M. Kuzmina, M. Herbig, D. Ponge, S. Sandlöbes, D. Raabe, Linear complexions: Confined chemical and structural states at dislocations, Science (80-.). 349 (6252) (2015) 1080–1083.
[66] G. Sha, A. Cerezo, Kinetic Monte Carlo simulation of clustering in an Al-Zn-Mg-Cu alloy (7050), Acta Mater. 53 (4) (2005) 907–917.
[67] T. Karahan, H. Ertek Emre, M. Tümer, R. Kaçar, Strengthening of AISI 2205 duplex stainless steel by strain ageing, Mater. Des. 55 (Mar. 2014) 250–256.